China Instrument and Control Society
Instrumentation
OPEN ACCESS
INSTRUMENTATION, Vol. 11, No. 3, September 2024 https://doi.org/10.15878/j.instr.202400192

Article

Brake Discs Surface Defect Detection Using the IGD-IHT Algorithm and the PIQEDS-ISSA-NESN Algorithm

Feng Li[1], Zhen Yu[2,3,*], Juan Gao[4], Qi An[5]

[1] Haier School (Electromechanical School), Qingdao Technical College, Qingdao Shandong 266555, China

[2] Institute of Oceanographic Instrumentation, Qilu University of Technology (Shandong Academy of Sciences), Qingdao Shandong 266061, China

[3] State Key Laboratory of Precision Measuring Technology and Instrument, Tianjin University, Tianjin 300072, China

[4] School of Informatics, Qingdao Technical College, Qingdao Shandong 266555, China

5 Department of Mechanical Engineering, Tsinghua University, Beijing 100084, China

[*] Corresponding author email: solseagull@163.com

Abstract: As one of the core parts, the brake discs directly impact the braking and safety performance of vehicles. Traditional surface detection methods of the brake disc have poor robustness due to their reliance on manual feature extraction. A detection instrument was designed to focus on the detection. The features were extracted using the improved Gaussian difference algorithm and Hough transform algorithm(IGD-IHT). An identification method for brake disc surface defects was designed in this paper based on the Perception-based Image Quality Evaluator and Dempster rule-improved sparrow search algorithm-Nonlinear echo state network(PIQEDS-ISSA-NESN) to better identify. It was shown in the experiment that the accuracy was more than 97%, the false alarm rate was less than 1.5%, and the false alarm rate was less than 1.5%.

Keywords: surface defectdetection; IGD-IHT algorithm; PIQEDS-ISSA-NESN algorithm; brake discs

Citation: Li, Feng, Zhen Yu, Juan Gao, and Qi An. "Brake Discs Surface Defect Detection Using the IGD-IHT Algorithm and the PIQEDS-ISSA-NESN Algorithm." Instrumentation 11, no. 3 (September 2024). https://doi.org/10.15878/j.instr.202400192.

0 Introduction

As one of the core parts, the brake disc ensures the car's braking effect[1-3]. It is generally made of gray cast iron. During the casting process, defects such as sand holes and air holes may appear on the surface of brake discs[4-6]. These surface defects may increase safety hazards[7,8]. At present, in actual production and processing, surface defects of brake discs are handily examined by quality controllers[9-11]. This method has drawbacks such as inferior accuracy and high work hardness, which makes inspection extremely difficult[12-14].

Many traditional computer vision methods have been proposed to achieve quality inspection and to achieve automatic brake disc surface defects inspection. Zou et al. detect the surface defects using a Kalman filtering method[15]. Chu et al. detect defects using scanning welds with structured light sensors[16]. These traditional methods depend on manual feature extraction, which leads to poor generalization ability and robustness of these traditional computer vision methods[17]. In recent years, neural network algorithms, especially radial basis function neural networks, have shown wide versatility and strong plasticity[18-20]. However, some small surface defects (such as trachoma) can easily disappear during training, which can lead to poor detection results[21-23].

This article addresses the shortcomings of existing automatic detection methods for surface defects on brake discs and designs an automated detection instrument. The improved Gaussian difference and improved Hough transform algorithm (IGD-IHT) were used to extract

brake disc defect features. A brake disc surface defect recognition method based on the fusion algorithm of no reference quality evaluation and Dempster rule, improved sparrow search algorithm, and nonlinear echo state network (PIQEDS-ISSA-NESN) was designed, achieving fast and automatic detection. The designed brake disc surface defects automatic detection method can simultaneously detect defect information in four directions of the tested object: up, down, left, and right. It is suitable for detecting surface defects on brake discs of various sizes and provides a new solution for automatic detection.

1 Detection system

1.1 Structural design of the system

An online detection system for brake disc surface defects based on a six-axis industrial robot and a visual measurement system was designed, which is used to detect various types of brake disc surface defects with a diameter of 100 mm to 500 mm. The designed system is shown in Fig.1, which mainly consists of six subsystems, including a six-axis industrial robot movement system, visual measurement system, brake disc clamping system, brake disc drive system, motor and industrial robot drive control system, and image acquisition and processing system.

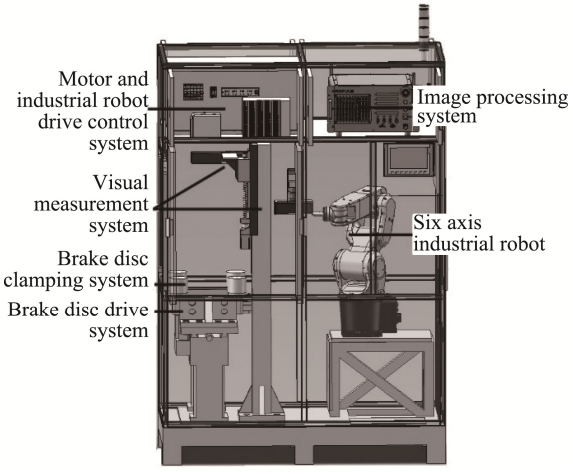

Fig.1 Structural design diagram.

The six-axis industrial robot mobile system mainly consists of six-axis industrial robots and guide rail moving components, which are fixed and installed on the base bracket to achieve the movement of the visual measurement system. It can be used to flexibly align the visual measurement system with the brake disc in four directions: up, down, left, and right. The visual inspection system mainly includes a bright line scanning light source, a 2D camera, and a line scanning lens, which are installed on the end effector of a six-axis industrial robot and the moving parts of the guide rail, respectively, for collecting surface images of brake discs. The brake disc clamping system consists of four adaptive rollers, one of which is the driving wheel and three are the driven wheels. The distance between the four rollers can be flexibly adjusted according to the diameter of the brake disc, and the clamping force can be adjusted through a hydraulic device to clamp the brake disc. The brake disc drive system is mainly composed of a private server motor, which can drive the driving wheel to rotate, thereby driving the brake disc to rotate through friction, and measuring as much as possible in the working state of the brake disc. The motor and industrial robot drive control system consists of a Programmable Logic Controller (PLC) and supporting circuits, used to control the precise movement of six-axis industrial robots, guide rail moving parts, and high-speed rotation of the brake disc drive system. The image acquisition and processing system consists of an industrial computer and supporting circuits, used for real-time acquisition of brake disc surface images captured by the visual measurement system, and completing brake disc surface defect detection.

1.2 Implementation process of surface defect detection for brake discs

The operation and measurement process of surface defect detection on brake discs are shown in Fig.2. Visual Studio 2022 was used as the software development platform, and the image acquisition and processing program, display, and storage program were programmed in C language. T-shaped diagrams for the motor and industrial robot drive control system were also written using the Botu V17 automatic stereoscopic warehouse. The entire process, except for manual feeding, is automatically completed by the six-axis industrial robot movement system and visual measurement system. The specific detection steps are as follows:

1. Manual loading, place the brake disc on the lifting platform in the center position of the clamping mechanism. 2. Start the equipment operation while ensuring personal safety. 3. The brake disc clamping system clamps the brake disc and plays a central positioning role (ensuring that the center point position of each brake disc is consistent). 4. The lifting platform has declined. 5. The brake disc drive system drives the brake disc to rotate. 6. The end effector of the robot drives the 2D line scanning camera and light source to move above the brake disc, automatically adjusting the brightness of the light source and taking pictures of the front (upper surface) of the brake disc. 7. After the front side image is taken, the robot moves to the side of the brake disc, and the camera takes a picture of the side of the brake disc. 8. After completing the side view, the robot moves to the opposite side of the brake disc, and the camera takes a picture of the opposite side (lower surface) of the brake disc. 9. After the 2D camera takes the image, the robot returns to the origin. 10. The brake disc drive system stops rotating. 11. After completing the

drawing, lift the platform. 12. The brake disc clamping system is released, and the brake disc is manually removed. 13. Perform image processing on all collected surfaces, complete surface defect detection on brake discs, and output results.

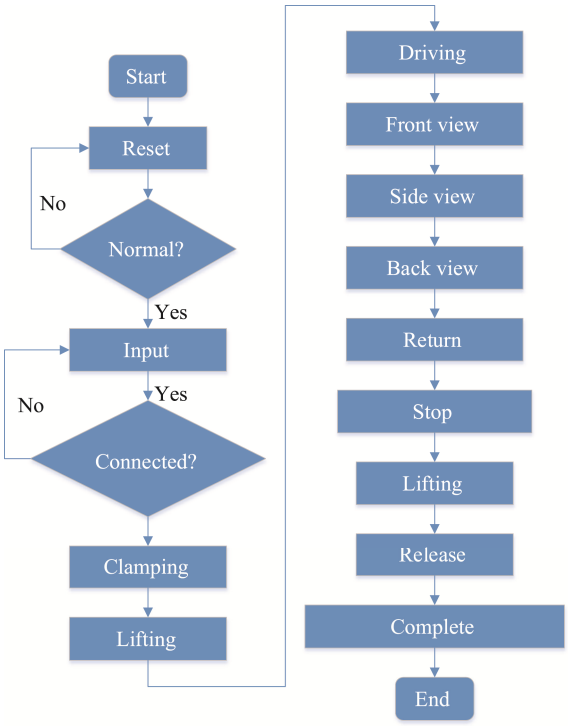

Fig.2 Flow chart for surface defect detection of brake discs.

2 Method for extracting surface defect features of brake discs

In response to the issue of online detection of brake disc surface defects, the previous section provides a detailed introduction to the structure and various components of the brake disc surface defect online detection system designed in this article and introduces the entire process of automatic completion of brake disc surface defect detection by the system. Regarding the process of detecting surface defects on brake discs, this section mainly introduces the method of extracting defect features from all collected surfaces. Three processing steps were mainly performed on the collected images: image enhancement, brake disc edge detection, and defect feature extraction to detect surface defects on brake discs. The improved Gaussian difference and Hough transform algorithm (IGD-IHT) were used to extract the defect features of brake discs. Below, we will provide a detailed introduction to each step.

2.1 Image enhancement based on improved Gaussian filtering algorithm

This article uses a visual measurement system to achieve non-contact measurement of surface defects on brake discs. The collected images of the four directions of the brake disc, including up, down, left, and right, carry all the surface defect information of the brake disc. Due to factors such as lighting and vibration, the original image is doped with noise. It is necessary to perform image preprocessing in advance to improve image clarity and to better extract the surface defect features of brake discs.

This article uses an improved Gaussian filtering algorithm to filter and enhance the collected brake disc surface images. The so-called improved Gaussian filtering algorithm is a smoothing filter based on Gaussian functions, which mainly filters out Gaussian noise in the image. The expression of the Gaussian filtering function in the improved Gaussian filtering enhancement method is:

$$f(u,v) = Ae^{-\frac{(u-u_0)^2+(v-v_0)^2}{2\sigma^2}} \tag{1}$$

The process of Gaussian filtering is to iteratively convolve the target image with a convolutional template, and use this template to traverse all regions of the image, thereby achieving a weighted average of the overall image. The so-called improved Gaussian filtering here first takes some measures to eliminate light saturation points before filtering. If the grayscale values of two or more consecutive pixels are saturated when scanning the target image row by row (column), then all light-saturated points do not participate in Gaussian filtering. If the grayscale value of the only pixel is saturated, the light saturation point participates in Gaussian filtering. After removing the light saturation point, further improvement lies in roughly calculating the number of pixels in the convolution kernel and the value of the center pixel. The number of pixels in the convolution kernel and the value of the center pixel are related to the mean and variance in the Gaussian filtering function. Based on the original convolution kernel width, scale it down proportionally and retain the remaining 5-9 pixels to participate in Gaussian filtering. Calculate the values of each pixel in the convolution kernel, select the peak extremum point and 2-4 points on its left and right sides, and use the grayscale centroid algorithm to solve for the value of the central pixel point. The central coordinates are:

$$\begin{aligned} u_1 &= u_0 - \frac{g_{u2} - g_{u3}}{g_{u1} + g_{u2} + g_{u3}}, \\ v_1 &= v_0 - \frac{g_{v2} - g_{v3}}{g_{v1} + g_{v2} + g_{v3}} \end{aligned} \tag{2}$$

In the above formula, u_1 and v_1 are the pixel coordinates of a certain grayscale extreme point along the u and v axes, respectively. g_{u1}, g_{u2}, g_{u3} correspond to the grayscale value of a point along the u-axis, while g_{v1}, g_{v2}, g_{v3} correspond to the grayscale values at a point along the v-axis.

2.2 Defect feature extraction based on improved Gaussian difference and improved Hough transform algorithm (IGD-IHT)

After improving the image clarity, it is necessary to first extract the edge features of the brake disc surface

image to facilitate the extraction of defect features. The edge features of the brake disc surface image, as one of the global features of the brake disc, can accurately convey the characteristics of surface defects on the brake disc, such as defect location, defect size, etc. It is crucial to develop an edge extraction algorithm based on actual brake disc surface features to improve the accuracy of extracting surface defects on brake discs. This article takes into account the surface images of brake discs collected by the visual measurement system under the illumination of a bright line scanning light source, and extracts edge features based on an improved Gaussian edge extraction algorithm. Finally, based on the improved Hough transform algorithm, pore-shaped defects such as trachoma and pores, as well as strip-shaped defects such as scratches and cracks were extracted.

2.2.1 Extracting edge features based on an improved Gaussian difference algorithm

An improved Gaussian difference algorithm is used in this article to extract edge features of brake disc images. In the Gaussian difference operation, the original grayscale image is convolved with Gaussian functions with different standard deviations to obtain the image filtering result, and the response image is obtained by subtracting the adjacent images in two Gaussian scale-spaces. Subtracting one image from another preserves the spatial information contained in the frequency bands of the two images. Through this method, Gaussian difference operation can achieve edge detection of images. The improved Gaussian difference algorithm is an approximation of the Gaussian Laplace algorithm, mainly combining Gaussian filtering and difference operation for edge detection. The expression of the two-dimensional Gaussian function used in it is:

$$G(w,\ s,\ \sigma)=\frac{1}{\sigma\sqrt{2\pi}}e^{-\frac{w^2+s^2}{2\sigma^2}} \tag{3}$$

Among them, w and s are the image coordinates, and σ is the standard deviation of the probability distribution. The Gaussian function is used to smooth images and two different σ values are taken for the Gaussian difference operation of two images. The Gaussian filtering result of the image is:

$$g_1(w,\ s)=G_{\sigma 1}(w,\ s)*f(w,\ s) \tag{4}$$

$$g_2(w,\ s)=G_{\sigma 2}(w,\ s)*f(w,\ s) \tag{5}$$

Finally, subtract the two filtered images g_1 and g_2 to obtain::

$$g_1(w,\ s)-g_2(w,\ s)=(G_{\sigma 1}(w,\ s)-G_{\sigma 2}(w,\ s))*f(w,\ s) \tag{6}$$

Among them, * represents convolution. That is to say, Gaussian difference operation can be expressed as:

$$g_1(w,\ s)-g_2(w,\ s)=\frac{1}{\sqrt{2\pi}}\left(\frac{1}{\sigma_1}e^{-\left(\frac{w^2+s^2}{2\sigma_1^2}\right)}-\frac{1}{\sigma_2}e^{-\left(\frac{w^2+s^2}{2\sigma_2^2}\right)}\right) \tag{7}$$

2.2.2 Extracting Pore and Strip Defects Based on Improved Hough Transform Algorithm

After extracting the edge features of brake disc images, this paper uses an improved Hough transform algorithm to extract pore-like defects such as sand holes and pores, as well as strip-like defects such as scratches and cracks. The main principle of using the improved Hough transform algorithm for extracting pore-shaped defects such as trachoma and pores is to detect trachoma and pores based on the highly symmetrical shape of the pore-shaped defect. The specific steps are as follows:

1. Read the improved Gaussian difference algorithm to extract edge features of brake disc images.

2. Scan from left to right and from top to bottom using a straight line to calculate the coordinates of the midpoint.

3. Repeat step 2 multiple times, taking the average of the coordinates of the intermediate point images obtained from multiple scans from left to right and top to bottom, and then taking the average of the coordinates of the intermediate point images obtained from scans from left to right and top to bottom. Finally, the coordinates of the intermediate point are obtained as the center coordinates of the elliptical circle where the hole-shaped defect is located.

4. Randomly select a certain number of points on the edge of a hole-like defect, input them into the elliptical equation, and calculate the elliptical parameters.

5. Repeat step 4 multiple times and take the average of the obtained multiple sets of elliptical parameters to obtain the final elliptical parameters.

The principle of using the improved Hough transform algorithm in extracting strip defects such as scratches and cracks is to use a two-stage cross-scanning method to identify two sampling points and whether the pixels between the sampling points can form a straight line, thereby determining whether the two sampling points have voting rights. The specific steps are as follows:

1. Discretize the image space and initialize the parameter space.

2. Randomly sample two pixels and use the two-stage scanning of core pixels method. The number of core pixel points between the two points is N, and the actual number of core pixel points between the two pixels is recorded as M. If $M/N>0.8$, the values in the corresponding parameter space are accumulated.

3. Repeat step 2 for K times.

4. Map the points in the parameter space that exceed the threshold to the image space, and perform least squares fitting on the line to obtain the slope and intercept.

5. Use the method of minimizing residuals to obtain the weight w.

6. The weight w is used to reconstruct the least squares fitting to obtain updated slopes and intercepts.

7. Determine whether the relative difference

between the two fitting coefficients is less than the tolerance. If the requirements are not met, repeat the above process.

8. Finally, output the optimal slope and intercept as coefficients for the centerline function.

From the above, it can be seen that the IGD-IHT algorithm replaces the ineffective sampling caused by randomly selecting two edge points in traditional Hough transform algorithms by scanning the core pixel points to filter out invalid sampling points. Compared with traditional Hough transform algorithms, the IGD-IHT algorithm method can significantly reduce outliers. By comparing the residuals of the elliptic equation and the linear equation obtained from the two methods, as shown in Table 1 and Table 2, it can be seen that the IGD-IHT algorithm can obtain the elliptic equation with a residual of 1.236×10^{-3} and the linear equation with a residual of 1.024×10^{-4}.

Table 1 Residual of elliptic equation fitting for porous defects.

Algorithm type	Traditional hough transform	IGD-IHT algorithm
Residual	7.85×10^{-2}	1.236×10^{-3}

Table 2 Residual of linear equation for fitting strip defects.

Algorithm type	Traditional hough transform	IGD-IHT algorithm
Residual	3.76×10^{-2}	1.024×10^{-4}

3 Real-time recognition method for surface defects of brake discs

According to the Gaussian difference algorithm and the improved Hough transform algorithm proposed in Part 3, the features of pore-shaped defects such as sand holes and pores, as well as strip-shaped defects such as scratches and cracks, can be extracted. After completing the defect feature extraction, it is also necessary to recognize the extracted features to identify the defect categories corresponding to different features. It is necessary to establish a standard database that includes defect feature information and category information to facilitate real-time recognition of images containing defect information captured by visual measurement systems. The steps of database creation mainly includes three steps: data collection, data annotation, expert verification, and correction. Considering that the effectiveness of defect feature extraction may vary under different lighting intensities, it is necessary to collect a large amount of data under different lighting intensities. After completing the collection of defect feature information, it is necessary to annotate the defect features and defect categories. This article uses category annotation software based on the PCL database to manually annotate the defect features and categories of each brake disc surface image.

After establishing the database, it is necessary to conduct training on identifying surface defects on brake discs. During the training process, it is necessary to first use the information in the database as the evidence set, and based on the Perception-based Image Quality Evaluator (PIQE) and Dempster (DS) rule fusion algorithm, perform confidence allocation and quality evaluation on the extracted features. After completing confidence allocation and quality evaluation, this article uses the ISSA algorithm to optimize defect features. Finally, the NESN neural network is used for training, with the extracted hole and strip defect features as input values and defect category information as expected output values, to obtain the relationship between defect category information and defect features. After completing the training, during the detection process, the surface defect category of the brake disc can be outputted in real time based on the extracted defect features. The defect recognition method will be described in detail below.

3.1 PIQEDS Algorithm

Considering the influence of factors such as lighting and vibration on the image, resulting in noise doping, the extracted surface defect feature information of brake discs has uncertainty. Therefore, confidence allocation is performed using the Dempster rule for information on hole-shaped defects and bar-shaped defects in the standard database. Specifically, it involves assigning basic confidence to the likelihood of an event occurring, and this step requires designing specific assignment methods based on the visual measurement system's decision algorithm. This article designs a confidence assignment method based on the characteristics of visual measurement systems and performs basic confidence assignment. The specific process is as follows:

Define an "identification framework" ψ that includes all events and define a credibility allocation function w:

$$w(\tau) = 0 \tag{8}$$

$$\sum_{b\subset\psi} w(b) = 1 \tag{9}$$

Among them, τ represents the impossible event and $w(b)$ represents the confidence level of defects b measured by the visual measurement system.

For events b, their confidence function can be defined as $Qel(b)$:

$$Qel(b) = \sum_{c\subset b} w(c) \tag{10}$$

The confidence function of b is the sum of the confidence levels of all subsets of b.

As mentioned earlier, the detection environment is susceptible to factors such as lighting and vibration, which can provide incorrect criteria for the DS rule fusion algorithm. Evidence conflicts may occur during the fusion process, seriously affecting the accuracy of the final fusion result. A trusted weight is set on the visual measurement system in the Dempster rule fusion stage to correct the evidence weight of the sensor on the fusion result and to eliminate the impact caused by imaging

quality so that the fusion algorithm has an adaptive ability to the surrounding environment. Specifically, it is to design a reference-free quality evaluation algorithm to evaluate the image and obtain an image quality evaluation value to judge the current visual measurement system's perception of the scene and set different trust weights for different scenes. The image quality evaluation value is a measure of the clarity and lighting intensity of the collected image, and the determination of the credibility weight is determined by the prior detection recall rate. The specific steps of the non-reference quality evaluation algorithm are as follows:

First, calculate the MSCN coefficients $\hat{i}(a,b)$ and divide them into N_x blocks of size $m \times m$ (m=18), using $\hat{i}(a,b)$ to mark whether each block is uniform or independent.

$$A_q = \begin{cases} W & \rho_q < 0.1 \\ TB & \rho_q \geqslant 0.1 \end{cases} \tag{11}$$

Where ρ_q is the variance of the MSCN coefficients for block A_q, $q \in 1, 2, ..., N_x$. Below is the evaluation quality score for the block.

There are two types of processing for block distortion: image clarity and exposure intensity.

In terms of clarity, for each M_o in the $m \times m$ block A_q, it is divided into 13 parts:

$$b_{oq} = M_o(a) : a = q, q+1, \cdots q+5 \tag{12}$$

$o \in 1, 2, 3, 4$ represent four edges, $q \in 1, 2, 3, \ldots, 13$ represent that each edge can be divided into 13 parts and each section is 5 in length. If any part of the standard deviation is less than a certain threshold, it is considered to have a problem of poor clarity, which satisfies

$$\sigma_{oq} < S \tag{13}$$

In terms of exposure intensity, the block is divided into a central area and a peripheral area, and the standard deviation is calculated as σ_c and σ_s, respectively. The standard deviation of the block is calculated as:

$$\sigma_\beta = \frac{\left| \frac{\sigma_c}{\sigma_s} - \alpha \right|}{\max \max \left(\frac{\sigma_c}{\sigma_s}, \alpha \right)} \tag{14}$$

If there is an exposure issue, there are the following relationships:

$$\sigma_\beta > 2\alpha \tag{15}$$

Distortion using ρ_q degree blocks:

$$C_{sk} = \begin{cases} 1 & if\ both\ (13)\ and\ (15)\ hold\ true \\ \rho_b & if\ (13)\ is\ established \\ 1-\rho_b & if\ (15)\ is\ established \end{cases} \tag{16}$$

The quality score of the entire image:

$$QP = \frac{\sum_{k=1}^{M_s} C_{sk} + D_1}{M_s + D_1} \tag{17}$$

Where D_1 is a constant and M_s is the total number of independent blocks.

After completing confidence allocation and quality evaluation, this article uses neural networks for training to obtain the relationship between defect category information and defect features. The features of hole-shaped defects and strip-shaped defects were optimized based on the ISSA algorithm to prevent getting stuck in local optima.

3.2 ISSA Algorithm

In this paper, the ISSA algorithm is used to optimize the points of a laser cross-section. The ISSA is a swarm intelligence algorithm proposed that searches for the optimal solution by simulating the group behavior of a sparrow. The sparrow population is mainly composed of producers and scroungers and has a detection and early warning mechanism. Among them, the producers mainly provide the foraging direction and area for the whole population, and the scroungers follow the producers for foraging, some sparrows, accounting for about 10% to 20% of the population, are responsible for monitoring the foraging area. It has the advantages of fast convergence speed and easy implementation[24]. The process is as follows:

If there are n sparrows in the population, then the population composed of all individuals can be expressed as $X=[x_1, x_2, \ldots, x_n]^T$, and the corresponding fitness function of each individual is $F=[f(x_1), f(x_2), \ldots, f(x_n)]^T$. Among them, the transposition formula is as follows:

$$x_{i,j}^{t+1} = \begin{cases} x_{i,j}^t \cdot exp\left(\frac{-i}{a \times iter_{\max}} \right) & if\ R2 < ST \\ x_{i,j}^t + Q \cdot L & if\ R2 \geqslant ST \end{cases} \tag{18}$$

In the above equations, t represents the current number of iterations, $x_{i,j}^t$ represents the position of the i sparrow in the j dimension at the t generation, $\alpha \in (0,1)$, $iter_{max}$ represents the maximum number of iterations, $R2$ represents the alarm value, ST represents the security threshold, Q is the random number obeying the normal distribution, L is the matrix of $1 \times dim$, dim represents the dimension. The producers' location update method can be summarized as follows: when $R2 < ST$, there are no predators around the feeding area, and the producers can search widely for food; When $R2 \geqslant ST$, predators appear and all producers need to fly to safety.

The scroungers follow the producers to find food and may compete with the producers for food, increasing the probability of their predation, and its position is updated in the following way:

$$x_{i,j}^{t+1} = \begin{cases} Q \cdot \exp\left(\frac{x_{worst}^t - x_{i,j}^t}{i^2} \right) & if\ i > n/2 \\ x_P^{t+1} + \left| x_{i,j}^t - x_P^{t+1} \right| \cdot A^+ \cdot L & if\ i \leqslant n/2 \end{cases} \tag{19}$$

In the above equations, x_{worst}^t is the individual position with the worst fitness in the t generation, and

x_P^{t+1} represents the individual position with the best fitness in the t+1 generation. A represents A matrix of 1×dim, in which each element is randomly preset to –1 or 1, at the same time $A^+= A^T(AA^T)^{-1}$. The producers' position update method can be summarized as When i>n/2, the i-th scroungers have low fitness and do not compete with the producers, so they need to fly to other areas for food. When i⩽n/2, the scrounger forages near the optimal individual X_P.

When the population forages for food, some sparrows are selected to be on the lookout, and when the enemy approaches, either the producers and scroungers abandon the current food or fly to another location. Sparrows with SD probability (generally 10%~20%) are randomly selected from each generation population for early warning behavior. Its position update formula is:

$$x_{i,j}^{t+1}=\begin{cases} x_{best}^t+\beta\cdot\left|x_{i,j}^t-x_{best}^t\right| & if\ f_i\neq f_g \\ x_{best}^t+k\cdot\left|\dfrac{x_{i,j}^t-x_{best}^t}{\left|f_i-f_w\right|+\varepsilon}\right| & if\ f_i=f_g \end{cases} \tag{20}$$

Where x_{best}^t is the global optimal position in the t iteration, β controls the step size and follows a normal distribution with mean 0 and variance 1. $k\in[-1, 1]$, ε is set to a constant to avoid denominators of 0. f_i indicates the fitness value of the current individual, f_g and f_w indicate the fitness value of the current global best and worst individual, respectively. The updating mode can be summarized as follows: When $f_i\neq f_g$, the individual is in the periphery of the population, so it needs to adopt anti-predation behavior and constantly change its location to obtain higher fitness. When $f_i=f_g$, the individual is at the center of the population, and it keeps approaching nearby peers to keep away from the danger zone.

The initialization of the sparrow population is very important for the convergence speed and optimization accuracy of SSA. Since there is no prior knowledge available at the initial stage of the sparrow group, the initial position of most swarm intelligence algorithms is randomly generated. The initial population is evenly distributed in the search space, which is of great help in improving the algorithm optimization.

The chaotic sequence has randomness, ergodicity, and regularity, and the sparrow population generated by it has good diversity. The basic idea is that the algorithm generates a chaotic sequence in the interval [0, 1] through a mapping relationship, and then transforms it into the individual search space. There are many ways to generate chaotic sequences. This paper uses the chaotic sequences generated by Logistics mapping to initialize the Sparrow algorithm population. The mathematical expression of Logistics mapping is as follows[25]:

$$y_{i+1}^j=\mu y_j^i(1-y_j^i)y_j^i<0.5 \tag{21}$$

In this paper, μ=4; i=1, 2, ... N represents population size; j=1, 2, ... d indicates the sequence number of chaos variable. The Logistics chaotic mapping is very sensitive to the selection of initial values, and *d–th* chaotic sequences y_j^i can be obtained by selecting *d–th* initial value with a slight difference. Then d-th chaotic sequences y_j^i are inversely mapped to the corresponding individual search space variable x_j^i.

$$x_j^i=lb_i+(ub_i-lb_i)y_j^i \tag{22}$$

Where, ub_i and lb_i are search boundaries.

In the sparrow search algorithm (SSA) algorithm, the scrounger chooses only one producer with a higher fitness value than himself for learning. Although this kind of random learning is conducive to the algorithm's exploration in the search space, the sudden decline of the diversity of the population leads to the decline of the algorithm's ability to jump out of the local optimal, resulting in the lack of optimization ability of the algorithm. Multidirectional learning strategies are adopted for the scrounger to solve this problem.

Suppose there are four solutions in a certain search space, where *b* is the local optimal solution, *o* is the global optimal solution, *a* and *c* are random solutions different from *b* and *o*. The multidirectional learning strategies are used to improve the follower position update formula to increase the diversity of the population, expand the search scope, and quickly approach the global optimal solution:

$$x_{i,j}^{t+1}=\begin{cases} Q\cdot\exp\left(\dfrac{x_{worst}^t-x_{i,j}^t}{i^2}\right) & if\ i>n/2 \\ \dfrac{\tau_a X_{a,j}^t+\tau_b X_{b,j}^t+\tau_c X_{c,j}^t}{\tau_a+\tau_b+\tau_c} & if\ i\leqslant n/2 \end{cases} \tag{23}$$

Among them, τ_a, τ_b, and τ_c represent the weight of individual sparrows at points *a*, *b*, and *c* respectively, and the specific expression is:

$$\begin{cases} \tau_a=\dfrac{f_a+f_b+f_c}{f_a} \\ \tau_b=\dfrac{f_a+f_b+f_c}{f_b} \\ \tau_c=\dfrac{f_a+f_b+f_c}{f_c} \end{cases} \tag{24}$$

Among them, f_a, f_b and f_c represent the fitness values of sparrows located at points a, b, and respectively, and different weights are obtained according to the fitness values, the weight is proportional to the fitness values. The position information of sparrows a, b, and c is comprehensively considered, and the global search ability of the algorithm is expanded.

The iterative process of the SSA algorithm is the process of getting closer to the optimal individual. If the current optimal individual is the local optimal, the search stagnation of the SSA algorithm is easy to occur. We introduced Cauchy variation and reverse learning strategy to mutate the optimal individual in the sparrow population to avoid the occurrence of this situation.

Reverse learning is used to find the corresponding reverse solution based on the current solution through the reverse learning mechanism, and then evaluate and compare the better-preserved solution. The reverse learning strategy is integrated into the Sparrow algorithm to enable individuals to better find the optimal solution, and the mathematical representation is as follows:

$$X'_{best}(t) = ub + r \oplus (lb - X_{best}(t)) \tag{25}$$

$$x_{i,j}^{t+1} = X'_{best}(t) + b_1 \oplus (X_{best}(t) - X?_{best}(t)) \tag{26}$$

Where, $X'_{best}(t)$ is the reverse solution of the optimal solution of the T generation, ub and lb are the upper and lower bounds respectively, r is a random number matrix of $1\times d$ (d is the spatial dimension) uniformly distributed following the standard (0,1), b_1 represents the information exchange control parameter, the formula is as follows:

$$b = (iter_{\max} - \frac{t}{iter_{\max}})^t \tag{27}$$

The Cauchy variation is derived from the Cauchy distribution, and the probability density of the one-dimensional Cauchy distribution is as follows:

$$f(x) = \frac{1}{\pi} \cdot \frac{a}{a + x^2} \tag{28}$$

In the equation above, $x \in (-\infty, +\infty)$. The Cauchy variation is introduced into the target position update mode, and the perturbation ability of the Cauchy operator is utilized to improve the global optimization performance of the algorithm.

$$x_{i,j}^{t+1} = X_{best}(t) + cauchy(0,1) \oplus X_{best}(t) \tag{29}$$

In the equation above, cauchy(0, 1) is the standard Cauchy distribution. The Cauchy distribution random variable generating function is $\eta = tan[(\xi - 0.5)\pi]$. A dynamic selection strategy is adopted to update the target position to further improve the optimization performance of the algorithm. The reverse learning strategy and the Cauchy mutation operator perturbation strategy are executed alternately under a certain probability to dynamically update the target position. The reverse learning strategy expands the search domain of the algorithm, and the Cauchy mutation strategy mutates the optimal individual in the sparrow population, which improves the convergence accuracy of the algorithm. The update selection of the target location is determined by the selection probability P, which is calculated as follows:

$$P_S = -exp(1 - \frac{t}{iter_{max}})^{20} + \theta \tag{30}$$

Where, θ is the adjustment parameter, and its value can be 0.05. After the update of perturbation variation, the greedy rule is introduced to determine whether to update the position by comparing the fitness values of the old and new positions. The greedy rule is shown in equation(31), where $f(x)$ represents the location fitness value of x.

$$X_{best} = \begin{cases} x_{i,j}^{t+1} & if\ f(x_{i,j}^{t+1}) < f(X_{best}) \\ X_{best} & if\ f(x_{i,j}^{t+1}) \geqslant f(X_{best}) \end{cases} \tag{31}$$

3.3 NESN Algorithm

After optimizing defect features using ISSA, this paper uses the NESN neural network for training. We will use ISSA-optimized hole and strip defect features as input values, and use defect category information as the expected output value to complete NESN neural network training and obtain the relationship between defect category information and defect features[26]. After completing the training, during the detection process, the surface defect category of the brake disc can be output in real-time based on the extracted defect features, thereby achieving real-time and rapid recognition of brake disc surface defects under vibration and various lighting conditions. It can significantly improve the accuracy of identifying surface defects on brake discs, and output frequency, and enhance the reliability of the system, achieving the best recognition effect of surface defects on brake discs.

This article uses nonlinear functions to establish the nonlinear relationship between the internal states of the reserve pool. The improved ESN is called the Nonlinear Echo State Network (NESN), and its structure is shown in Fig.3. Compared with ESN, NESN increases the readout layer by $M=p\times q$ units.

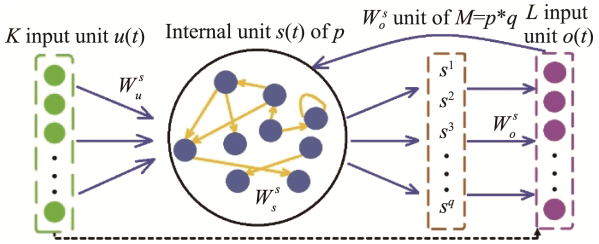

Fig.3 NESN Network Structure

At the time t, the dimensions of the input connection weight matrix W_u^s and the internal connection weight matrix W_s^s in the reserve pool decrease accordingly. The connection weight matrix W_o^s between the readout layer and the output layer is $L\times(p\times q)$, and the feedback connection weight matrix W_o^s from the output layer to the reserve pool is $p\times L$. Compared with the standard ESN, NESN significantly reduces the dimensions of internal connection weights and feedback connection weights in the reserve pool under the precise dimension of internal state, thereby correspondingly reducing the complexity of model computation.

$$o(t) = f_{out}(W_s^o \cdot s(t)) \tag{32}$$

$$s^q(t) = [s_1^q(t), s_2^q(t), s_3^q(t), \cdots, s_p^q(t)]^T \tag{33}$$

$$s(t) = [s^1(t), s^2(t), s^3(t), \cdots, s^q(t)]^T \tag{34}$$

4 Surface defect detection experiment

4.1 Implementation details

In order to verify the PIQEDS-ISSA-NESN algorithm, a brake disc surface defect detection experiment was conducted using the online detection system based on a six-axis industrial robot and visual measurement system designed in this paper. The experimental process is shown in Fig.4. According to the detection steps described in the second part of this article, surface defects were detected in the upper, lower, left, and right directions of the brake disc. In the actual testing process, the brake discs tested were the Brebo 08.E368 series brake discs. Nine types of brake discs with diameters from 100 mm to 500 mm were tested. Before starting the inspection, system parameters were set based on the size of all brake discs and the presence of defects, and a standard database containing defect feature information and category information was established. Then, the PIQEDS-ISSA-NESN algorithm proposed in this article was used for training, and the relationship between surface defect category information and defect features of brake discs of various sizes was obtained. Before training, the ISSA algorithm was used to optimize the extracted defect features. Set the overall particle size of the ISSA algorithm to 50, the learning factor $c_1=c_2=2$, and w is dynamically updated by formula (24), rand1＝0.5，rand2＝0.6. Due to the impact of the selection of iteration times on training time, the maximum iteration time is preset to 1000. During training, it was found that the fitness of the ISSA algorithm was stable after 300 iterations, so the maximum number of iterations was set to 300. In the experiment, a total of 90 independent repeated experiments were conducted on nine types of brake discs, and the first 80 sets of data were selected for training the NESN neural network. After completing the training, all 90 sets of data were tested to verify the effectiveness of online recognition of surface defects on brake discs.

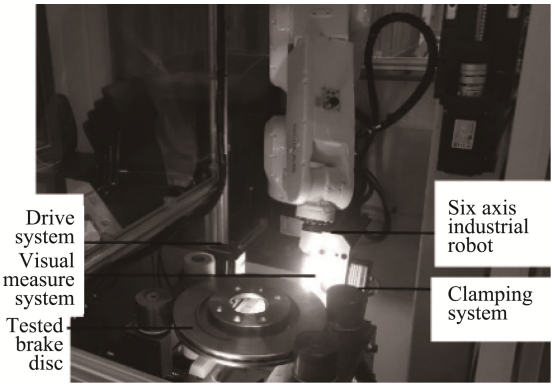

Fig.4 Surface defect detection experiment

The experiment was conducted in the online detection system for surface defects of brake discs designed in this article. The six-axis industrial robot used in the system is the XB7 industrial robot produced by Luoshi Company, with a repeated positioning accuracy of 50 microns. The guide rail used is a 16-5T3 guide rail, with a repeated positioning accuracy of 50 microns. The PLC used is the H5U series product produced by Huichuan Company, the servo motor used is the SV630 series product produced by Huichuan Company, the 2D industrial line scanning camera used is the A-CAM-CCG-4010-00 camera produced by Dalsa Company, with a scanning accuracy of 7.04 microns, the industrial lens used is the VCT7180-M lens produced by OPT Company, the industrial line scanning light source used is the VCT6060-3H light source produced by OPT Company, and the industrial computer used is the TANK-870-Q170i-i7-7700t industrial computer produced by IEI Company, with a memory of 16 GB and a maximum main frequency of 2.9 Hz, which can be used to quickly complete image processing. The above hardware system can fully meet the needs of online real-time detection of surface defects on brake discs.

4.2 Experimental verification of defect feature extraction effect

In order to better verify the impact of defect extraction on the defect recognition performance of brake discs, we compared the defect feature extraction method based on the Gaussian difference algorithm and the improved Hough transform algorithm proposed in this paper with some mainstream feature extraction methods (sift feature extraction method and Hough transform feature extraction method). Unlike commonly used defect feature extraction methods that can only consider information from a limited neighborhood, the feature extraction method can obtain more defect features by repeatedly extracting them. 90 sets of feature data extracted by the methods used in this article and mainstream methods were respectively fed into the proposed brake disc surface defect recognition algorithm based on the PIQEDS-ISSA-NESN algorithm for defect recognition. The experimental results are shown in Table 3. It can be seen that compared with mainstream defect feature extraction methods, the defect feature extraction method based on the Gaussian difference algorithm and improved Hough transform algorithm has the highest accuracy in defect recognition.

Table 3 Effect of defect feature extraction

Algorithm type	Defect identification accuracy	False alarm rate	Underreporting rate
Sift feature extraction method	88.9%	6.7%	4.4%
Hough transform feature extraction method	83.3%	8.9%	7.8%
The method described in this article	97.8%	1.1%	1.1%

4.3 Defect recognition effect inspection experiment

The proposed brake disc surface defect recognition algorithm based on the PIQEDS-ISSA-NESN algorithm was compared with some mainstream defect recognition methods (RBF neural network-based defect recognition method and BP neural network-based defect recognition method). Taking the recognition of surface defects on brake discs with a diameter of 300 mm as an example, the surface defect features extracted using the defect feature extraction method in this paper were applied to three different methods for defect recognition. The effectiveness of using the method described in this article to identify defects on each end face of brake discs is shown in Fig.5. Considering the limited space of this article, only a comparison of defect recognition effects using three methods for the most difficult-to-detect inner end face is shown in Fig.6.

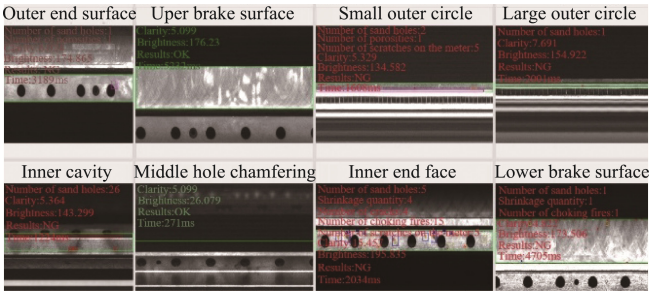

Fig.5 Experimental results of detecting surface defects on brake discs

(a) This article's method (b) RBF neural network (c) BP neural network

Fig.6 Comparison of defect recognition effects using three methods for inner end faces

From Figs.5 and 6, it can be seen that the defect recognition method proposed in this paper can quickly achieve real-time detection and recognition of defects on all end faces of brake discs. Compared with mainstream defect recognition methods, the defect recognition method proposed in this paper can accurately identify defects of different sizes on brake discs. Meanwhile, by using ISSA to optimize defect features, the NESN network can better identify defect category information.

We compared our method with mainstream defect recognition methods on the brake disc surface defect dataset. For a fair comparison, we used the defect feature extraction method in this article to extract the surface defect features of brake discs and optimized the surface defect features of brake discs using the ISSA algorithm. After optimization, 80 sets of defect feature data were fed into three neural networks for training. After completing the training, all 90 sets of data were tested to verify the effectiveness of online recognition of surface defects on brake discs. The experimental results are shown in Table 4.

Table 4 Defect Identification Effect

Algorithm type	Defect identification accuracy	False alarm rate	Underreporting rate
The method described in this article	97.8%	1.1%	1.1%
Defect recognition method based on RBF neural network	84.4%	8.9%	6.7%
Defect recognition method based on BP neural network	75.6%	13.3%	11.1%

From Table 4, it can be seen that the defect recognition method based on the BP neural network has the lowest accuracy in defect recognition, followed by the defect recognition method based on the RBF neural network. The proposed brake disc surface defect recognition method based on the PIQEDS-ISSA-NESN algorithm performs the best and has the highest accuracy in defect recognition. The error of the PIQEDS-ISSA-NESN algorithm is 23% higher than that of the BP neural network for defect recognition accuracy. It can be seen that the PIQEDS-ISSA-NESN algorithm has an accuracy rate of>97%, a false alarm rate of<1.5%, and a false alarm rate of<1.5%. In the same training environment, the method described in this article is superior to other neural networks and has significant advantages in improving the accuracy of brake disc surface defect recognition.

5 Conclusion

In response to the shortcomings of existing automatic detection methods for brake disc surface defects, this paper designs an automated detection instrument based on machine vision. The IGD-IHT algorithm was used to extract brake disc defect features. A brake disc surface defect recognition method based on the PIQEDS-ISSA-NESN algorithm was proposed to better detect surface defects on brake discs, which achieved rapid and automatic detection of brake disc surface defects. The experimental results show that the accuracy is>97%, the false alarm rate is<1.5% and the false alarm rate is<1.5%. The designed automatic detection method for surface defects on brake discs can quickly detect defect information in four directions: up, down, left, and right of the tested object. The contribution of this article is that this method can be applied to real-time online detection of surface defects on brake discs of various sizes, providing a new solution for the automatic detection of surface defects on brake discs.

Author Contributions:

Feng Li (First Author): Conceptualization, Methodology, Software, Investigation, Funding acquisition, Formal analysis, Writing - Original Draft.

Zhen Yu (Corresponding Author): Conceptualization, Funding Acquisition, Resources, Data curation, Supervision, Writing - Review & Editing.

Juan Gao: Writing - Review & Editing, Supervision, Investigation, Validation, Formal Analysis, Visualization.

Qi An: Methodology, Software, Writing - Review & Editing, Investigation, Supervision.

Funding Information:

This research work was bankrolled by the West Coast New Area University President Fund Special Project of Qingdao Technical College (Grant No.39100101), the National Key Research and Development Plan (Grant No.2017YFF0108100), the Basic Research Projects of Science, Education, and Industry Integration Pilot Project of the Qilu University of Technology (Shandong Academy of Sciences) (Grant No. 2023PX031), the Natural Science Foundation of Qingdao under Grants No. 23-2-1-121-zyyd-jch, and the project ZR2023QE212 supported by Shandong Provincial Natural Science Foundation.

Data Availability:

The authors declare that the main data supporting the findings of this study are available within the paper and its Supplementary Information files.

Conflict of Interest:

The authors declare no competing interests.

Dates:

Received 5 June 2024; Accepted 19 September 2024; Published online 30 September 2024

References

[1] Wei L, Choy Y S, Cheung C S. A study of brake contact pairs under different friction conditions with respect to characteristics of brake pad surfaces[J]. *Tribology International*, 2019, 138: 99–110.

[2] Ma Q H, Wang Y. Fault diagnosis and analysis of hydraulic brake based on friction vibration signal[J]. *Journal of Vibroengineering*, 2023, 25(5): 908-920.

[3] Yuan B, Liao D, Jiang W, et al. Effect of tool tilt angle on microstructure, mechanical properties and fracture behavior of dissimilar friction stir lap welding joint of SiCp/ZL101 and ZL101[J]. *Journal of Materials Research and Technology*, 2023, 23: 4642-4662.

[4] Zhang Y H, Liu Y, Wang J K, et al. Microstructure and wear resistance of direct laser-deposited TiC-enhanced aluminum-based composite coating for brake discs[J]. *Surface and Coatings Technology*, 2023, 455: 129193.

[5] Chen X T, Lu C, Mo J L, et al. Evolution of High-temperature Wear Mechanism of Railway Train Brake Friction Block Considering Frictional Heat br[J]. *China Surface Engineering*, 2023, 36(3): 142-151.

[6] Sun M, Chen S Y, Wei M W, et al. Preparation of 24CrNiMoY alloy steel with high strength and toughness by selective laser melting[J]. *Powder Metallurgy*, 2023, 66(5): 403-415.

[7] Zhang P, Li J C, Zhao Y, et al. Crack propagation analysis and fatigue life assessment of high-strength bolts based on fracture mechanics[J]. *Scientific Reports*, 2023, 13(1): 14567.

[8] Wang Z X, Jia Z Y. Development of High Accurate Family-use Digital Refractometer Based on CMOS[J]. *Instrumentation*, 2023, 3: 12-22.

[9] Zhen Y, Yuan Z. Diagnosis of the coupling misalignment of the vertical comprehensive performance test instrument of high precision reducer for industrial robot[J]. *Measurement*, 2021, 185: 109939.

[10] Zhu H Y, Lian S R, Jin M Z, et al. Review of research on the influence of vibration and thermal fatigue crack of brake disc on rail vehicles[J]. *Engineering Failure Analysis*, 2023, 153: 107603.

[11] Wang H T, Liu X. Research on Rotating Machinery Fault Diagnosis Based on Improved Multi-target Domain Adversarial Network[J]. *Instrumentation*, 2024, 1: 38-50.

[12] Yu Z, Qiu Z R, Li H, et al. Measuring the no-load running torque of RV reducer based on the SVD and MCSA[J]. *Measurement*, 2022, 190: 110697.

[13] Seo H, Lee D G, Park J, et al. Quench hardening effect of gray iron brake discs on particulate matter emission[J]. *Wear*, 2023, 523: 204781.

[14] Kumar P K D, Gnanaraj S D. Aluminium-Silicon based Metal Matrix Composites for brake rotor applications: a review[J]. *Engineering Research Express*, 2023, 5(2): 022002.

[15] Zou Y, Du D, Chang B, et al. Automatic weld defect detection method based on Kalman filtering for real-time radiographic inspection of spiral pipe[J]. *NDT & E International*, 2015, 72: 1–9.

[16] Chu H H, Wang Z Y. A vision-based system for postwelding quality measurement and defect detection[J]. *International Journal of Advanced Manufacturing Technology*, 2016, 86(9-12): 3007–3014.

[17] Chen M, Yu L, Zhi C, et al. Improved faster R-CNN for fabric defect detection based on Gabor filter with genetic algorithm optimization[J]. *Computers in Industry*, 2022, 134: 103551.

[18] Yu Z, Xu P F, Li H, et al. The decelerator tester twisting distortion caused angular measurement error calibration, based on the IBSCF-SGDPSO-RBF method[J]. *Measurement*, 2023, 207: 112374.

[19] Zhen Y, Zurong Q, Hao L, et al. Design and Calibration of Torque Measurement System of Comprehensive Performance Test Instrument of Industrial Robot Reducer[J]. *Computational Intelligence and Neuroscience*, 2022, 2022: 81558188.

[20] Zhen Y, Wancheng Y. Shafting Misalignment Malfunction Quantitative Diagnosis Based on Speed Signal SVD-HT and CSF-PPSO-ESN Method[J]. *Computational Intelligence and Neuroscience*, 2022, 2022: 7016597.

[21] Krizhevsky A, Sutskever I, Hinton G E. ImageNet Classification with Deep Convolutional Neural Networks[J]. *Association for Computing Machinery*, 2017, 60(6): 84–90.

[22] Chen F C, Jahanshahi M R. NB-CNN: Deep Learning Based Crack Detection Using Convolutional Neural Network and Naive Bayes Data Fusion[J]. *IEEE Transactions on Industrial Electronics*, 2018, 65(5): 4392–4400.

[23] Su B, Chen H, Zhou Z. BAF-detector: An efficient cnn-based detector for photovoltaic cell defect detection[J]. *IEEE Transactions on Industrial Electronics*, 2022, 69(3): 3161-3171.

[24] Hongyan X, Qiang Z, Chunxia L U. Adaptive stochastic resonance method for weak signal detection based on particle swarm optimization[J]. *Instrumentation*, 2015, 2: 3-10.

[25] Jane C J. An Application of Pareto Particle Swarm Optimization Using with Geographic Information System Technology[J]. *International Journal of Kansei Information*, 2014, 5(1): 13-17.

[26] Lemos T, Campos L F, Melo A, et al. Echo state network based soft sensor for monitoring and fault detection of industrial processes[J]. *Computers & Chemical Engineering*, 2021, 155: 107512.